






RESEARCH ARTICLE | SEPTEMBER 20 2024

Spatially resolved Thomson scattering measurements of electron properties across the acceleration region of a high-power magnetically shielded Hall effect thruster


Julian Lopez-Uricoechea  ; Jean Luis Suazo Betancourt ; Naia Butler-Craig ; Mitchell L. R. Walker 


 Check for updates


J. Appl. Phys. 136, 113303 (2024)


<https://doi.org/10.1063/5.0213928>




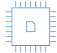
 Nanotechnology & Materials Science

 Optics & Photonics

 Impedance Analysis


 Scanning Probe Microscopy

 Sensors

 Failure Analysis & Semiconductors

Unlock the Full Spectrum.
From DC to 8.5 GHz.
Your Application. Measured.

[Find out more](#)



Spatially resolved Thomson scattering measurements of electron properties across the acceleration region of a high-power magnetically shielded Hall effect thruster

Cite as: J. Appl. Phys. **136**, 113303 (2024); doi: [10.1063/5.0213928](https://doi.org/10.1063/5.0213928)

Submitted: 14 April 2024 · Accepted: 1 September 2024 ·

Published Online: 20 September 2024



View Online



Export Citation



CrossMark

Julian Lopez-Urcochea,^{a)} Jean Luis Suazo Betancourt, Naia Butler-Craig, and Mitchell L. R. Walker

AFFILIATIONS

School of Aerospace Engineering, Georgia Institute of Technology, Atlanta 30318, Georgia

^{a)} Author to whom correspondence should be addressed: jlopezur3@gatech.edu

ABSTRACT

Noninvasive measurements of electron properties in a Hall effect thruster (HET) are needed to understand the physical processes in the acceleration region and to validate simulations. This paper presents spatially resolved laser Thomson scattering (LTS) measurements across the entire acceleration region of a HET. The test article is the H9, a 9 kW class magnetically shielded HET. The H9 is operated on krypton at a facility pressure of 1.2×10^{-5} Torr Kr (1.6 mPa). The thruster is operated at three discharge conditions: 171 V, 35 A, an inner coil current (I_{ic}) of 4.11 A, and an outer coil current (I_{oc}) of 2.27 A as the baseline 6 kW condition; 154 V, 34.8 A, an I_{ic} of 4.11 A, and an I_{oc} of 2.27 A to vary the discharge voltage; and 171 V, 34.4 A, an I_{ic} of 4.52 A, and an I_{oc} of 2.5 A to vary the magnetic field strength. At each discharge condition, we measured axial profiles of electron density and electron temperature along the channel centerline from 5% to 95% of a channel length downstream of the channel exit plane. At the baseline condition, we also measure the axial profile of the azimuthal electron drift velocity. We measure a minimum electron density of $1.3 \times 10^{17} \text{ m}^{-3}$, peak electron temperatures around 40 eV, and a peak azimuthal electron drift velocity around 680 km/s. The results suggest the presence of anomalous electron heating and demonstrate that low discharge voltages allow LTS to access the entire acceleration region of a HET.

© 2024 Author(s). All article content, except where otherwise noted, is licensed under a Creative Commons Attribution (CC BY) license (<https://creativecommons.org/licenses/by/4.0/>). <https://doi.org/10.1063/5.0213928>

INTRODUCTION

A Hall effect thruster (HET) is an electrostatic thruster that generates a cross-field discharge that accelerates ions for thrust primarily in the axial direction.¹ While there is no fully predictive model for HET operation, decades of testing have advanced HETs to the point where they are currently the most used type of propulsion on satellites. Accurate experimental measurements of ion and electron properties are crucial for the development of fully predictive HET models because such measurements can be used to validate simulations and help advance the theory of anomalous phenomena in HETs.^{2–9} A fully predictive HET model would be able to accurately predict the performance and lifetime of a HET based only on a HET's design and would be valuable for the rapid design optimization of HETs at different power levels and on different propellants.

Accurate measurements of electron properties in the acceleration region of a HET are of particular importance for the validation of simulations. The acceleration region is the quasineutral region in the thruster discharge with a strong axial electric field. Anomalous electron mobility is largely responsible for determining the spatial variation of the axial electric field,^{6,7} and the axial profile of the axial electric field is then directly related to the voltage utilization efficiency of a HET.^{7,10} Anomalous electron mobility also increases the electron current, which decreases the current efficiency of a HET.¹⁰ Thus, understanding anomalous electron mobility is critical in the development of a fully predictive HET model. To address this need, laser-induced fluorescence (LIF) measurements have been used to calibrate simulations^{6,7} for the axial profile of anomalous electron collision frequency or, in one case, to directly infer⁵ the axial profile of anomalous electron collision frequency.

20 September 2024 16:08:35

These axial profiles have been used to check theories of anomalous electron mobility with limited success.^{6,11–14}

While it is likely that this limited success is due to the theories needing to be corrected, it is important to note that most theories of anomalous electron mobility depend on the local electron properties.¹² Specifically, models of anomalous electron collision frequency often rely on a combination of electron density, electron temperature, and azimuthal electron drift velocity, among other plasma properties.^{12,13} Consequently, accurate values of these electron properties in the acceleration region are needed to properly check theories against axial profiles of anomalous electron mobility.

Optical techniques are generally preferred over probe techniques for accurate measurements of plasma properties because they are noninvasive, in that they do not perturb the plasma.² LIF has become a standard noninvasive technique in HET research for measuring ion and neutral properties.^{15–22} At the same time, Langmuir probes are the standard in HET research for point measurements of electron properties.²³ Incoherent laser Thomson scattering (LTS) is an established practice in plasma research for noninvasive point measurements of density, electron temperature, and electron drift velocity. Still, until technological advancements in the last decade, LTS systems needed more sensitivity to measure the acceleration region of the HET.²⁴

Recent LTS measurements in the acceleration region of HETs show electron temperatures that greatly exceed those expected from simulations and Langmuir probe measurements.^{24,25} As a result, to make the most of axial profiles of anomalous electron collision frequency, these profiles should be accompanied by LTS measurements of axial profiles of electron temperature. Additionally, accurate axial electron temperature profiles across the acceleration region could be compared to results from calibrated simulations to gain insights into anomalous electron heating. Also, while not previously demonstrated, the authors believe that LTS measurements of the azimuthal electron drift velocity can be used to calibrate simulations for anomalous electron mobility.

An important caveat is that this potential capability of LTS is only valid if LTS can access the entire acceleration region. Multiple studies have shown a downstream shift of the acceleration region with a decreasing discharge voltage,^{4,19,26} and magnetic shielding also shifts the acceleration region downstream with respect to conventional HETs.^{19,24,27} Recent LTS measurements on the magnetically shielded H9 operating at 300 V were not able to access the entire acceleration region.²⁵ However, LTS on a magnetically shielded HET operating at 150 V was able to measure across the entire acceleration region.²⁸ This indicates that magnetically shielded HETs should provide LTS access to the entire acceleration region at low discharge voltages.

In this study, we present axial profiles of electron density, electron temperature, and azimuthal electron drift velocity on a magnetically shielded HET with a recently implemented LTS diagnostic.²⁹ All these electron properties were measured at the baseline discharge condition of 171 V, 35 A, an inner coil current (I_{ic}) of 4.11 A, and an outer coil current (I_{oc}) of 2.27 A. Axial profiles of electron density and electron temperature were also measured at the discharge conditions of 154 V, 34.8 A, an I_{ic} of 4.11 A, and an I_{oc} of 2.27 A and of 171 V, 34.4 A, an I_{ic} of 4.52 A, and an I_{oc} of 2.5.

The study has three objectives regarding axial profiles of LTS measurements along the channel centerline of a HET. First, we want to demonstrate that LTS can measure across the entire acceleration region of the H9 at the chosen discharge conditions. Second, we want to see whether our LTS diagnostic has the sensitivity to capture the expected axial profiles of electron density, electron temperature, and azimuthal electron drift velocity across the acceleration region. Third, we want to see whether the LTS diagnostic has the sensitivity to capture the expected differences in the axial profiles of electron density and electron temperature due to 10% variations in the discharge voltage and applied magnetic field strength. We will use the measured axial profiles of the electron temperature and azimuthal electron drift velocity to determine whether LTS is able to measure across the entire acceleration region. Section II describes the experimental setup of the HET and the LTS diagnostic. Section III presents the theory and procedures used for processing the recorded LTS spectra. Section IV presents noninvasive axial profiles across the acceleration region of electron density, electron temperature, and azimuthal electron drift velocity at a single discharge condition and axial profiles of electron density and electron temperature at two other discharge conditions. We discuss the results in terms of the expected profiles across the acceleration region and the expected differences between the discharge conditions.

EXPERIMENTAL SETUP

Section II A describes the vacuum test facility in which the experiment was conducted. Section II B presents the setup of the H9 HET and the operating conditions, and Sec. II C presents the LTS diagnostic.

Vacuum test facility

The experiment was conducted in Vacuum Test Facility 2 (VTF-2) at the High-Power Electric Propulsion Lab (HPEPL) at Georgia Tech. VTF-2 is 9.2 m long and 4.9 m in diameter. A 495 CFM rotary-vane pump is used to reach 5 Torr (666.5 Pa); at this point, Raman scattering on this residual air is performed to calibrate the LTS diagnostic. A 3800 CFM blower is then used to reach rough vacuum of around 10 mTorr. Ten IN2-cooled CVI TMI reentrant cryopumps are used to reach high vacuum with a pumping speed of 390 000 l/s on krypton in this experiment. For this experiment, VTF-2 achieved a base pressure of 8.7×10^{-9} Torr N₂ (1.2 μ Pa) and an operating pressure of 1.2×10^{-5} Torr Kr (1.6 mPa) at a Kr flow rate of 369 SCCM.

We used a Kurt J Lesker XCG-BT-FB-1 capacitance manometer with a range of 1000–1 Torr (1.333×10^5 to 133.3 Pa) to measure the chamber pressure during the Raman scattering measurements. At high vacuum, the chamber pressure was monitored with three Agilent Bayard-Alpert 571 hot-filament ion gauges at separate locations inside the chamber, and the reported pressure is the average of the three ion gauges.

Hall thruster test setup and operation

The study was performed on the H9, a 9 kW class magnetically shielded HET with a LaB₆ center-mounted cathode.³⁰ The Jet

Propulsion Laboratory, the University of Michigan, and the Air Force Research Laboratory designed the H9, which has a boron nitride channel. The H9 was chosen for this experiment because magnetic shielding pushes the acceleration region outside of the discharge channel,^{19,24,27} which may allow the LTS diagnostic to probe across the entire acceleration region.

Research-grade (99.999% purity) krypton was supplied to the anode via an MKS GE50A00650S8V020 mass flow controller and to the cathode via an MKS GE50A006102S8V020 mass flow controller. The mass flow controllers are calibrated by measuring the flow upstream of the thruster with a MesaLabs DryCal 800-10 volumetric flow meter. The anode flow rate was 345.34 ± 3.27 SCCM, and the cathode flow rate was 23.71 ± 3.89 SCCM.

The H9 discharge was powered with a Magna-Power TSA800-54 power supply. To prevent discharge current oscillations above 1.4 kHz from going into the discharge power supply, a filter with a 95 μ F capacitor and a 1.3 Ω resistor is connected to the discharge power supply. The discharge voltage is measured in the control room at a location in the thruster circuit between the discharge filter and the thruster. The discharge current and its oscillations are measured by a Teledyne LeCroy CP150 current clamp connected to a Teledyne LeCroy HDO6104 oscilloscope at a sampling rate of 1 MS/s for 1 s. The thruster body is isolated from ground and is configured to be electrically floating.

The thruster operating conditions used in this experiment are shown in Table I. The polarity of the magnet coils was configured to create a magnetic field predominantly in the negative radial direction at the location of the maximum magnetic field strength. When changing the magnetic field strength, the ratio of the currents through the inner and outer coils was kept constant such that the magnetic field topology was kept constant. 10% variations in magnetic field strength and discharge voltage were chosen so that the dominant discharge current oscillation mode did not change across the operating conditions.^{31,32} In this manner, the changes in the measured electron properties could be attributed to changes in the discharge voltage and applied magnetic field strength. The H9 was operated at a high current density to increase the signal-to-noise ratio of the LTS measurements since the LTS signal is proportional to electron density. LTS measurements were taken when the discharge had reached steady-state, determined by waiting until the discharge current peak-to-peak dropped below 5 A.

It should be noted that the experiment was conducted over 2 days and that the discharge current at the baseline condition on the second day was 34.5 A. This is a 1.4% drop in discharge current, around an order of magnitude smaller than our controlled

10% variations of the discharge condition and is within the uncertainty of the LTS measurements. As a result, the 1.4% drop in discharge current should not affect the LTS measurements or the differences observed in the measurements with the controlled changes of the discharge condition.

To probe different locations in the H9 discharge, the H9 was moved with respect to the fixed LTS observation volume. The H9 was mounted atop three motion stages, which allowed three-directional movement of the thruster. To move the H9 in the $x_{chamber}$ and $z_{chamber}$ directions, as defined in Fig. 1, we used two Parker 4062000XR motion stages, and to move in the $y_{chamber}$ direction, as described in Fig. 1, we used an Optics Focus MOZ-300-150.

Thomson scattering setup

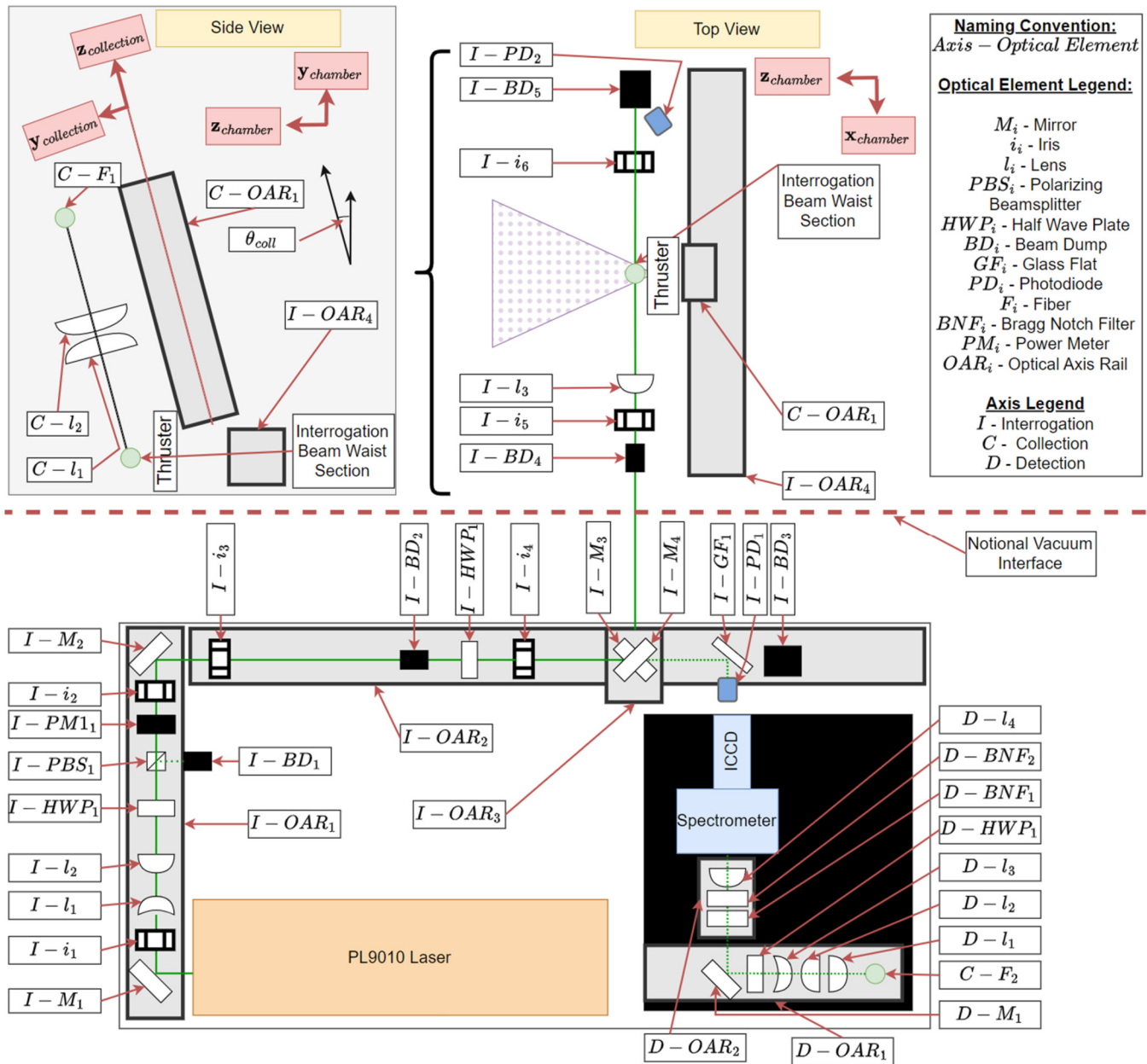
Thomson scattering is the elastic scattering of electromagnetic radiation off free charged particles. For low-density plasmas, only Thomson scattering from free electrons is considered, since Thomson scattering from free ions can be neglected due to the Thomson scattering cross section scaling as the inverse of the mass.³³

An LTS diagnostic is typically composed of three primary optical systems: the interrogation beam optical system, the collection optical system, and the detection optical system. The interrogation beam system generates the incident radiation with a laser and focuses the incident laser beam at the observation volume, which produces intense scattering at the observation volume. The observation volume is the portion of the incident laser beam imaged by the collection system. If an optical fiber is used as in our setup, then the collection system images the scattered light from the observation volume to the face of the fiber and transports the collected light to the detection system via the optical fiber. Alternatively, if no optical fiber is used, the collection system can be directly coupled with the detection system. If no optical fiber is used, then the collection and detection systems can be treated as one combined system, as done in Ref. 34. An optical fiber was used in this work because of the large distance between the observation volume and the spectrometer due to the size of the vacuum chamber. The detection optical system filters out the light near the wavelength of the interrogation beam. It images the light from the optical fiber to the slit of a spectrometer that is coupled to a detector. The detector then records the spectrum of the collected light. Before the commercialization of volume Bragg notch filters (BNFs), triple grating spectrometers,³⁵ gas cells, and

20 September 2024, 16:08:35

TABLE I. Operating conditions and azimuthal locations at which LTS was measured. For discharge conditions, the facility pressure was 1.2×10^{-5} Torr Kr (1.6 mPa), the anode flow rate was 345.34 ± 3.27 SCCM, and the cathode flow rate was 23.71 ± 3.89 SCCM. The probed azimuthal locations are shown in Fig. 2.

Probed azimuthal location	Discharge voltage (V)	Discharge current (A)	Inner coil current (A)	Outer coil current (A)	Discharge current peak-to-peak (A)
3 o'clock	171.3	35.00	4.11	2.27	4.49
3 o'clock	154.3	34.75	4.11	2.27	4.90
3 o'clock	170.6	34.37	4.52	2.50	4.18
12 o'clock	171.3	34.5	4.11	2.27	4.66



20 September 2024, 16:08:35

FIG. 1. Master optical diagram for the interrogation beam, collection, and detection optical systems. θ_{coll} is the angle between $y_{chamber}$ and $z_{collection}$. Adapted with permission from Suazo Betancourt *et al.*, J. Appl. Phys. **135**, 083302 (2024). Copyright 2024 Jean Luis Suazo Betancourt (Ref. 29).

polychromators were used to filter out the light around the laser wavelength.³⁵ Figure 1 shows the three optical systems.

The laser source used in the interrogation beam optical system was an Amplitude DLS Powerlite 9010 injection seeded, Q-switched Nd:YAG laser. The laser is operated with a second harmonic generator that outputs a 532 nm laser beam with a 9 mm

beam width and a beam pulse width between 5 and 8 ns. The laser is rated for a maximum output energy of 1J/pulse with a 10 Hz repetition rate. Still, internal laser misalignments meant that the laser was outputting around 650 mJ/pulse throughout this study. The beam goes through a 1.5:1 beam expander formed by the lenses I-1₁ and I-1₂ so as not to damage the polarizing beam splitter

cube, I-PBS1. The polarizing beam splitter cube has a rated polarization purity of 1000:1. The polarizing beam splitter cube and the half-wave plate I-HWP₁ modulate the beam power together, which is measured by a power meter on a flip mount, I-PM₁. The beam then passes through a second half-wave plate, I-HWP₂, to control the polarization of the incident light in the observation volume. Once the collection and detection systems are aligned, the orientation of the second half-wave plate is optimized to maximize Rayleigh scattering. To align the beam with the interrogation beam optical axis defined inside VTF-2, the beam goes through a periscope formed by the mirrors I-M₃ and I-M₄. The interrogation beam then enters VTF-2 via a custom Torr Scientific NSQ1462-25 KF-flanged Brewster window. Once the incident polarization at the observation volume was optimized without the Brewster window in place, the Brewster window was then oriented to minimize reflections at the window. Inside VTF-2, the beam is focused onto the observation volume with a 600 mm focal length lens, I-L₃, resulting in a beam width of around 100 μm in the observation volume. For more details on the interrogation beam optical system and the alignment practices, see Ref. 29.

The collection optical system forms a 1:1 image of the observation volume at the fiber face with two 350 mm focal length 150 mm diameter lenses, C-L₁ and C-L₂. A custom Thorlabs FG200LEA-FBUNDLE fiber bundle in a 7 × 1 array of 200 μm diameter FG200LEA multimode fibers transports the collected light to outside VTF-2 via a custom SQS Fiber Optics HEM048727 4.5 in. CF flange. A second set of the same custom fiber bundle then transports the collected light from the flange to the detection system. The collection system was designed to maximize the solid angle of the collection lens, C-L₁, with the constraints of a 1:1 imaging system to maintain high spatial resolution and that the numerical aperture of the focusing lens, C-L₂, was less than that of the multimode fiber, such that the entire 0.14 sr solid angle of the collection lens is used. Apart from determining the focal lengths and diameters of the lenses of the collection system, the design requirement of using all of the 0.14 sr solid angle also led to the collection axis being subtended at a 17° angle, as shown in the side view in Fig. 1. To be able to correct for small chamber movements between atmosphere and high vacuum, the fiber bundle is placed atop three motorized stages. To protect the collection optics from deposits from sputtering, the optics were put inside a box with an AR-coated glass flat placed at the front of the box. For more details on the collection optical system and the alignment practices, see Ref. 29.

In the detection optical system, the light exiting the optical fiber bundle is first collimated by a 150 mm focal length lens, D-L₁, and then passes through a 2:1 beam reducer formed by D-L₂ and D-L₃. Due to the beam reducer, all the collected light is able to pass through the two 25 mm OptiGrate OD-4 BNFs. The filtered light is then focused onto the entrance slit of the spectrometer with a 75 mm focal length lens, such that the magnification of the detection optical system is 2. This is the minimum magnification that would allow for maximum light throughput through the detection system, given that the numerical aperture of the spectrometer is just under half that of the multimode fibers. The spectrometer slit width is set to 500 μm to maximize light throughput at the cost of a lower spectral resolution. Our setup uses a Princeton Instruments

ISOPLANE-320A spectrometer coupled to a Princeton Instruments PM4-1024i-HB-FG-18-P46 PIMAX4 camera. For more details on the detection optical system and the alignment practices, see Ref. 29 and Ref. 36 for more information on the BNFs.

Figure 2 shows the scattering configuration. Because the collection axis is at a 17° angle in the axial direction from the y_{chamber} direction, all observation wavevectors in this setup have an axial component. The observation wavevector is defined as $\vec{k} = \vec{k}_s - \vec{k}_i$, where \vec{k}_i is the wavevector of the incident light and \vec{k}_s is the wavevector of the scattered light, which is colinear with the collection optical axis. As shown in Table I, at each discharge condition, we made an axial profile at the 3 o'clock channel centerline position, and at the baseline discharge condition, we made a separate axial profile at the 12 o'clock channel centerline position. Although the observation wavevector is the same at both azimuthal locations in terms of the chamber coordinate system, the observation wavevectors are different in the thruster's cylindrical coordinate system. Because of the subtended collection axis, the observation wavevectors have components in the thruster exit plane and perpendicular to the exit plane. The components of the observation wavevectors perpendicular to the exit plane are $k_{1,\perp} = k_1 \sin(17^\circ) \hat{z}$ and $k_{2,\perp} = k_2 \sin(17^\circ) \hat{z}$. In the thruster exit plane, the observation wavevectors are given by $k_{1,\parallel} = k_1 \cos(17^\circ) \cos(45^\circ) (\hat{r} + \hat{\theta})$ and $k_{2,\parallel} = k_2 \cos(17^\circ) \cos(45^\circ) (\hat{r} - \hat{\theta})$. The normalized observation wavevectors can then be written in the thruster's cylindrical

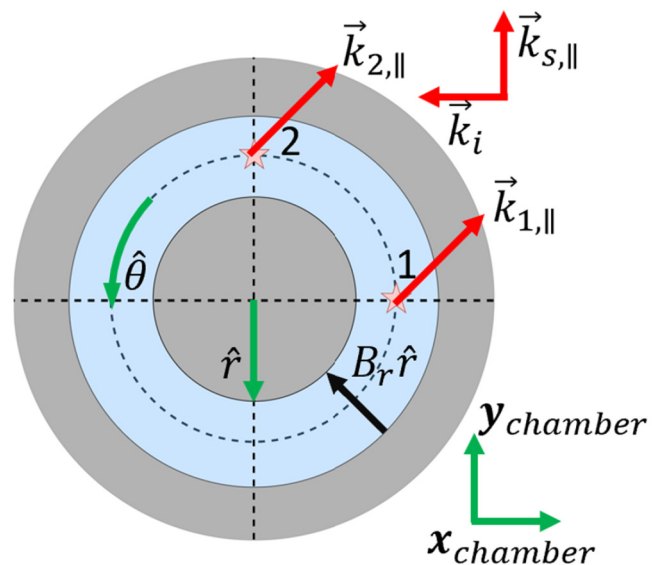


FIG. 2. LTS scattering configuration. Wavevectors projected onto the thruster exit plane, denoted by \parallel , are shown in red. The chamber coordinate system and the thruster's azimuthal and radial directions are shown in green. The radial component of the magnetic field is shown in black. The 3 o'clock azimuthal position is denoted as position 1, and the 12 o'clock azimuthal position is denoted as position 2. Incident and scattering wavevectors are positioned arbitrarily to show the relative orientation of \vec{k}_i and \vec{k}_s . Because of the subtended collection axis, $\vec{k}_{s,\parallel} = \cos(\theta_{coll})k_i y_{chamber}$.

20 September 2024, 16:08:35

coordinate system as

$$\frac{\vec{k}_1}{k_1} = \sin(17^\circ)\hat{z} + \cos(17^\circ)\cos(45^\circ)(\hat{r} + \hat{\theta}), \quad (1)$$

$$\frac{\vec{k}_2}{k_2} = \sin(17^\circ)\hat{z} + \cos(17^\circ)\cos(45^\circ)(\hat{r} - \hat{\theta}). \quad (2)$$

Due to preliminary testing with our ICCD, the minimization of the read noise of the detector guided our acquisition strategy. For each acquisition, we acquired 3000 shots, corresponding to an acquisition time of 5 min. At each point, we maximized the number of on-ccd accumulations, which was limited by the strongest emission line. The on-ccd accumulations varied between 100 and 1000. Our detector has a 1024×1024 imaging array, but our acquisition was done by vertically on-chip-binning the center 300 pixels. A bin height of 300 pixels was chosen to include the image of all seven fibers.

DATA PROCESSING FOR THOMSON SPECTRA

Thomson scattering is incoherent when the condition $\frac{2\pi}{k} \gg \lambda_{De}$ is satisfied, where λ_{De} is the Debye length and k is the observation wavenumber.²⁹ The observation wavenumber is given by²⁹

$$k \approx \frac{4\pi}{\lambda_i} \sin\left(\frac{\theta_{CI}}{2}\right), \quad (3)$$

where λ_i is the incident wavelength and θ_{CI} is the angle between the interrogation beam axis and the collection optical axis, which is 90° in our setup. The incoherent condition is met for the plasma conditions in this study, so we will only consider incoherent Thomson scattering going forward.

When the incident laser beam incoherently scatters off free electrons, the scattered radiation is Doppler shifted from the laser's wavelength according to the velocities of the electrons in the direction of the observation wavevector. As a result, the recorded spectrum of the scattered light is directly related to the electron velocity distribution function (EVDF) along the observation wavevector of the electrons in the observation volume. The spectral density of the photon counts in the signal measured from Thomson scattering as a function of wavelength is given as²⁹

$$P_s(\lambda) = \eta \frac{\lambda_i}{hc} E_i L_{det} \Delta\Omega n_e \frac{d\sigma^T}{d\Omega} S_k^T(\lambda), \quad (4)$$

where η is an efficiency constant, E_i is the incident laser energy, h is Planck's constant, c is the speed of light, L_{det} is the length of observation volume along the axis of the interrogation beam, $\Delta\Omega$ is the detection solid angle, n_e is the electron density, $\frac{d\sigma^T}{d\Omega}$ is the differential Thomson cross section, and $S_k^T(\lambda)$ is the Thomson spectral form factor as a function of wavelength. The angles between the collection axis, interrogation beam axis, and incident polarization vector were configured to maximize the Thomson cross section

such that it is given by²⁹

$$\frac{d\sigma^T}{d\Omega} = r_e^2 = \left(\frac{1}{4\pi\epsilon_0} \frac{e^2}{m_e c^2}\right)^2, \quad (5)$$

where r_e is the classical electron radius, e is the elementary charge, m_e is the electron mass, and ϵ_0 is the permittivity of free space.

Assuming a Maxwellian EVDF along the observation wavevector and neglecting the instrument broadening on the Thomson spectrum, $S_k^T(\lambda)$ is given as²⁹

$$S_k^T(\lambda) = \frac{\sqrt{2\pi}c}{k\lambda^2\sigma_k} \exp\left(-\frac{1}{2} \frac{(v(\lambda) - v_k)^2}{\sigma_k^2}\right), \quad (6)$$

where the index of refraction is assumed to be 1, v_k is the electron drift velocity along the observation wavevector, and σ_k and $v(\lambda)$ are given by²⁹

$$\sigma_k = \sqrt{\frac{eT_{eV,k}}{m_e}}, \quad (7)$$

$$v(\lambda) = \frac{\left(\frac{2\pi c}{\lambda_c} - \frac{2\pi c}{\lambda}\right)}{k}, \quad (8)$$

where $T_{eV,k}$ is the electron temperature in eV along the observation wavevector direction and λ_c is the wavelength on the detector at which the Thomson spectrum is centered if $v_k = 0$.

Equations (3)–(8) can be fit to the acquired Thomson spectrum without any calibration of the LTS system for $T_{eV,k}$ and for relative values of n_e and v_k . To use Eqs. (3)–(8) to fit for the absolute electron density, the system must be calibrated to find η . To use Eqs. (3)–(8) to fit for the absolute electron drift velocity, the system must be calibrated to find λ_c . We assume that $\lambda_i = 532$ nm and that the difference between λ_c and λ_i is due to small misalignments in the detection system. However, we note that λ_i could differ from 532 nm by ± 0.5 nm due to small misalignments in the laser cavity.

This study calibrates the LTS diagnostic with laser Raman scattering (LRS). Rotational Raman scattering is used instead of Rayleigh scattering to calibrate the LTS diagnostic because the detection optical setup is the same for both LRS and LTS. Furthermore, because the detection and collection optical setups are the same for both LRS and LTS, we use LRS to calibrate the product $\eta L_{det} \Delta\Omega$ instead of just η . To calibrate with Rayleigh scattering, the BNFs must be temporally removed, which would slightly change η .²⁹ In general, LRS can be used to find η if the gas pressure is known, and it can be used to find λ_c if the gas is static. In this experiment, LRS calibration is done at a facility pressure of 5 Torr (666.5 Pa), assuming a residual gas composition of 79% N_2 and 21% O_2 . For details on the model equations for LRS, see Ref. 29.

An axial profile at the 12 o'clock channel centerline position was done to indirectly measure the azimuthal electron drift velocity at the baseline discharge condition. To calculate the azimuthal electron drift velocity from the drift velocities at the 3 o'clock and

12 o'clock azimuthal positions, we note that from Eqs. (1) and (2),

$$\hat{\theta} = \frac{\vec{k}_1/k_1 - \vec{k}_2/k_2}{2 \cos(17^\circ) \cos(45^\circ)}, \quad (9)$$

such that

$$v_{e\theta} = \frac{v_{k1} - v_{k2}}{2 \cos(17^\circ) \cos(45^\circ)}. \quad (10)$$

It is important to clarify the meaning of the measured electron temperature when the LTS observation wavevector has some combination of axial, azimuthal, and radial components. To fit a 1D Maxwellian on an LTS spectrum collected at such an observation wavevector, we can assume the electron temperature is isotropic. Alternatively, given that the electron temperature in a HET is known to be anisotropic,²⁴ the reported electron temperature can be well approximated by

$$T_{ek} = T_{ez}\eta_z^2 + T_{e\theta}\eta_\theta^2 + T_{er}\eta_r^2, \quad (11)$$

where T_{ez} , $T_{e\theta}$, and T_{er} are the electron temperatures in the axial, azimuthal, and radial directions, respectively, and η_z , η_θ , and η_r are the normalized components of the observation wavevector. In our setup, $|\eta_z| = 0.292$ and $|\eta_\theta| = |\eta_r| = 0.676$. In this case, the reported electron temperature is approximately the average of the azimuthal and radial electron temperatures.

To obtain the LTS spectrum, four spectra must be acquired for each point. This is done to isolate the Thomson signal from the other sources of signal, such as plasma emission, stray light, and the detector DC bias. Spectrum A is the laser on, plasma on condition; spectrum B is the laser off, plasma on condition; spectrum C is the laser on, plasma off condition; and spectrum D is the laser off, plasma off condition. We will refer to the spectrum resulting from subtracting spectrum B from spectrum A as spectrum AB. We will refer to the spectrum resulting from subtracting spectrum D from spectrum C as spectrum CD. We will refer to the spectrum resulting from subtracting spectrum CD from spectrum AB as spectrum ABCD. Spectrum AB contains signal due to Thomson and stray light, and spectrum CD contains signal due to stray light, such that spectrum ABCD should only contain signal due to LTS.

However, during the experiment, we collected stray light that is not repeatable and, thus, distorts the LTS spectra. Importantly, this unrepeatable stray light is dispersed such that it cannot simply be ignored with a rejection region, as is done for the stray light due to reflections around 532 nm. The dispersed stray light is stronger farther away from the thruster, so we suspect that the main source of the unrepeatable stray light is fluorescence from the beam dump inside VTF-2. We suspect that it mainly originates from the beam dump because if we treat the beam dump as a light source, then as we move the thruster backward ($-z_{\text{chamber}}$ direction) to probe farther away from the thruster, more of the divergent rays of this light source can reflect off the front face of the thruster and into the collection optics. In addition, we suspect that this unrepeatable stray light is due to fluorescence because fluorescence spectra depend on temperature, and we took the A and C spectra at different thermal conditions. The A spectra were with the thruster on,

while the C spectra were taken with the thruster off. Additionally, we acquired the C spectrum at each location with less frames and later scaled the signal accordingly and alternated between C and D acquisitions. So, because of the higher heat loads from the thruster and the laser, we expect the beam dump to have been at higher temperature for the A spectra. For future experiments, we will change the setup to prevent light originating at the beam dump from being transmitted through our collection optics.

As shown in Fig. 3, we observe that, in the spectral range covered by the spectrometer of 517–546 nm, the unrepeatable stray light follows a consistent trend described by

$$P_{\text{stray}}(\lambda) = P_0 + \begin{cases} 0, & \lambda < \lambda_0 \\ m(\lambda - \lambda_{\text{stray}}), & \lambda \geq \lambda_0 \end{cases}, \quad (12)$$

where P_0 , λ_0 , and m are fitting parameters. In a previous experiment, we noticed a near constant dispersed light across the ABCD spectrum, so we believe that P_0 has some contribution from fluorescence from the front face of the thruster. Because m increases with distance from the thruster, we believe that it is related to fluorescence from the beam dump. The difference in temperature in the beam dump and thruster between the A and C spectra also influences the fluorescence spectra, and it is possible that this effect is captured by λ_0 . Ideally, if the spectrum of the beam dump is known, this could be incorporated into the fit on the ABCD spectrum with an additional fitting parameter that scales the fluorescence spectrum and that represents the probability that fluorescence photons enter the collection system. However, we do not know the temperature that the beam dump was at, so we cannot confidently use an available fluorescence spectrum, and we are currently not able to reproduce the thermal conditions of the beam dump to measure the fluorescence spectrum. Consequently, using

20 September 2024, 16:08:35

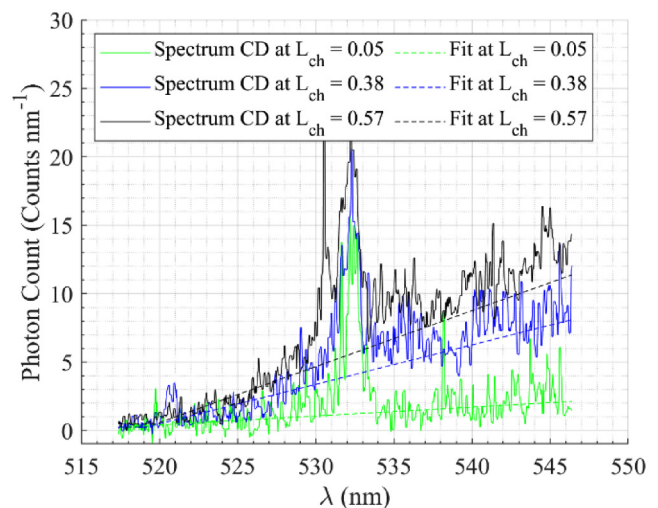


FIG. 3. CD spectra and the resultant fits from Eq. (12) for three different axial locations at the 3 o'clock azimuthal position.

Eq. (12), we implement a self-consistent method, described below, to account for this unwanted signal in our LTS spectra.

The beam dump's absorber is made of silicon carbide, and we have not found fluorescence spectra of this compound in the literature to support the validity of Eq. (12) within the spectral range considered. However, in a similar LTS setup as ours, described in Ref. 37, they presented the stray light spectrum over a wide spectral range in Fig. 5.6 (we note that their caption is mislabeled and that the green line is the stray light spectrum). They recovered the expected bell-shaped curve with a lower limit below the induced wavelength, and within the spectral range relevant for LTS, the fluorescence spectrum in Ref. 37 is approximately linear.

In addition, in Fig. 3, we observe larger oscillations in the stray light spectra at larger wavelengths. While this can be associated with issues regarding ICCD cooling, we do not know the origin of these fluctuations. Due to these fluctuations and other nonlinear dispersive behavior, small distortions to the LTS spectra may be introduced that limit our ability to analyze non-Maxwellian features in the EVDFs. As a result, resolving the inconsistency in the stray light spectra will be necessary for using our setup for detailed studies of non-Maxwellian phenomena. However, using Eq. (12), we implement a self-consistent method, described below, to account for the inconsistent stray light that allows us to obtain reliable Maxwellian fits on our data.

Equation (12) is first fit to spectrum CD, ignoring the center 16 nm. Equation (12) fit for spectrum CD is then subtracted from spectrum CD to create spectrum CD'. An iterative method is then used to account for the disperse stray light in ABCD.

When fitting Eq. (12) to spectrum ABCD, we use the value of λ_0 found for spectrum CD. As an initial correction for the stray light on spectrum ABCD, Eq. (12) is fit to spectrum ABCD, ignoring the center 30 nm. This fit is then subtracted from spectrum ABCD to create spectrum ABCD', where ABCD' is a supposed LTS spectrum. The LTS model equations, Eqs. (3)–(8), are then fit onto ABCD', ignoring the centered stray light. This LTS fit is then subtracted from spectrum ABCD to create spectrum E, which is the supposed dispersed stray light spectrum. Equation (12) is then fit onto spectrum E, ignoring the centered stray light, and this new Eq. (12) fit is then subtracted from spectrum ABCD to create a new ABCD' spectrum. The LTS model equations are fit onto this new ABCD' spectrum, and this process is then iterated until the LTS fitting parameters converge with a tolerance of 1%. Figure 4 shows an ABCD spectrum with the corresponding ABCD' and E spectra and the LTS fit resulting from the iteration.

Accounting for non-repeatable dispersed stray light is critical for obtaining accurate LTS results, even if the stray light signal is low. If stray light is over-subtracted on one side of the ABCD spectrum, this will artificially decrease the LTS signal on that side of the spectrum, which will reduce the calculated electron temperature and shift the calculated drift velocity away from the over-subtracted side of the spectrum. Over-subtracted disperse stray light can be easily identified if one of the wings of the LTS spectrum has many negative values. Similarly, if stray light is under-subtracted on one side of the spectrum, this will artificially increase the LTS signal on one side of the spectrum, which will increase the calculated electron temperature and shift the calculated drift velocity toward the under-subtracted side of the spectrum. Additionally, an artificial

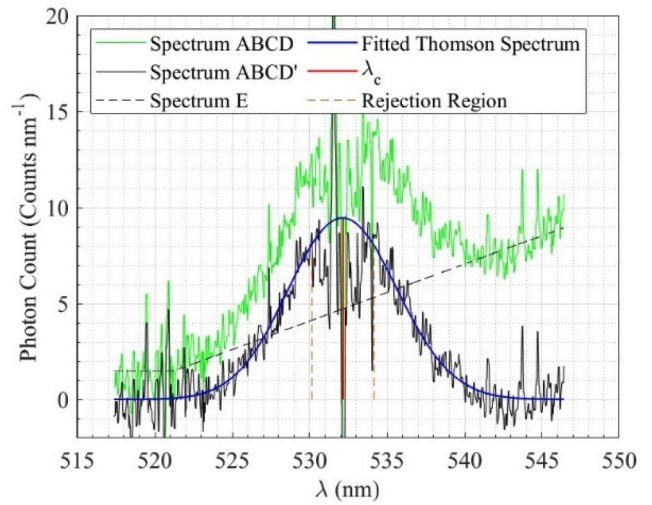


FIG. 4. Processed LTS spectrum and LTS fit at 0.69 of a channel length downstream of the thruster exit plane and at the 3 o'clock azimuthal location. Other spectra are shown to show the steps of data processing.

increase in the calculated electron temperature will cause an artificial decrease in the calculated electron density.

Error propagation and the residuals from the fits on the LTS and LRS spectra are used to calculate the uncertainty in the calculated electron properties. From each fit, a 95% confidence interval is calculated for each fitted parameter. The uncertainty for the electron temperature is directly taken from the 95% confidence interval of T_{eV} on the LTS fit. The uncertainty for the electron density is a combination of the 95% confidence intervals of n_e on the LTS fit and of η on the LRS fit, such that

$$\Delta n_e = \sqrt{(\Delta n_{e,LTS})^2 + \left(\frac{n_e}{\eta} \Delta \eta\right)^2}. \quad (13)$$

The uncertainty in the electron drift velocity along the observation wavevector is a combination of the 95% confidence intervals of v_k on the LTS fit and of λ_c on the LRS fit, such that

$$\Delta v_k = \sqrt{(\Delta v_{k,LTS})^2 + \left(\frac{2\pi c}{k} \left(\frac{1}{\lambda_c} - \frac{1}{\lambda_c + \Delta \lambda_c}\right)\right)^2}. \quad (14)$$

The uncertainty in the azimuthal drift velocity is given by

$$\Delta v_{e\theta} = 0.7394 \sqrt{\Delta v_{k,1}^2 + \Delta v_{k,2}^2}. \quad (15)$$

In addition, in our setup, the spectrometer has a resolution of 0.0288 nm, which corresponds to a drift velocity resolution of 11.5 km/s.

20 September 2024, 16:08:35

RESULTS AND DISCUSSION

This section presents noninvasive axial profiles of electron density, electron temperature, and the azimuthal electron drift velocity from 5% to 95% of a channel length downstream of the channel exit plane. For the data presented in this section, the distance from the exit plane is normalized by the discharge channel length, L_{CH} . The electron density and electron temperature measurements were made at the three conditions in Table I with an azimuthal location of 3 o'clock. In Sec. IV A, we present the measured electron density profiles, and Sec. IV B presents the measured electron temperature profiles. Section IV C presents the azimuthal electron drift velocity profile at the baseline discharge condition. Along with the profiles, we discuss how the profiles and differences between discharge conditions compare to those expected in the acceleration region of a HET.

We demonstrate that we mostly meet the objectives of the study. We show that LTS can measure across the entire acceleration region at the chosen discharge conditions. The shapes of the measured axial profiles of electron density, temperature, and azimuthal drift velocity agree with theory. The measured profiles of electron density and electron temperature agree with the expected differences with a change in discharge voltage. However, the measured axial profiles of electron density and electron temperature show no general trend with an increase in magnetic field strength, which we discuss can result from operating near the optimal magnetic field strength.

Figure 5 shows that the three discharge conditions have a strong peak in the power spectral density of the discharge current, which is indicative of the breathing mode. For the baseline condition, the peak frequency is 7 kHz, while for the other two conditions, the peak frequency is at around 6.5 kHz. This corresponds to a drop in peak frequency of around 7%. In Table I, the discharge current peak-to-peak changes by approximately 10%. As a result, the changes in the

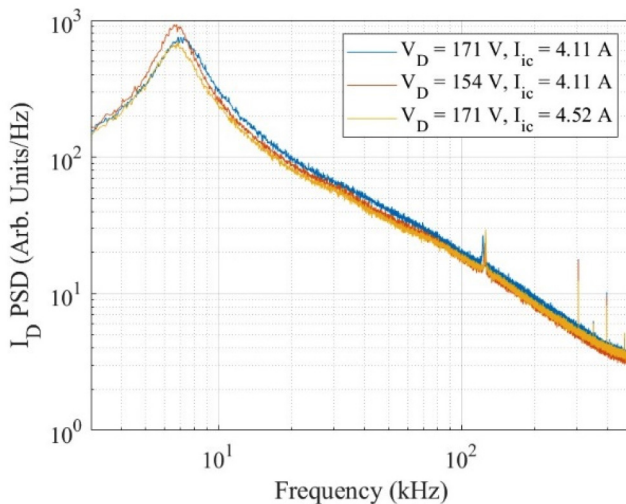


FIG. 5. Power spectral density of the discharge current at the three operating conditions.

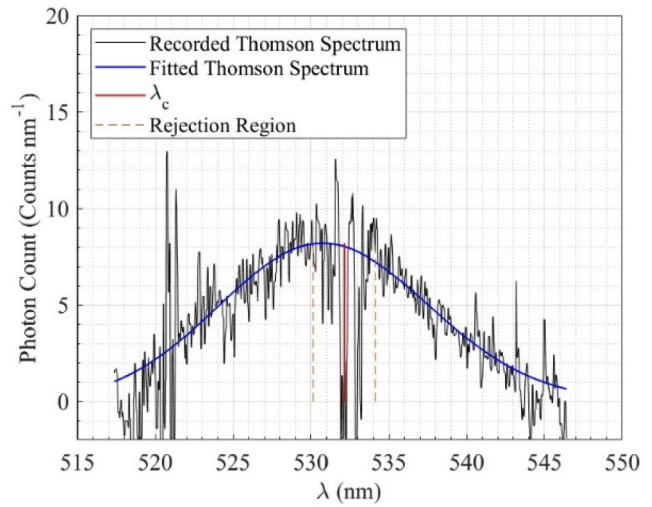


FIG. 6. Processed LTS spectrum and Thomson fit at 0.3 channel lengths downstream of the thruster exit plane and at the 3 o'clock azimuthal location.

measured electron properties with discharge condition can be attributed to changes in the discharge voltage and magnetic field strength instead of to changes in the stability regime of the discharge.

In Fig. 6, the Maxwellian fit agrees well with the recorded LTS spectrum. The wings of the Thomson fit are the regions that do not agree as well with the recorded LTS spectrum. In Fig. 7, we provide the raw LTS spectrum at the closest point to the thruster without the correction for the inconsistent stray light. At this location, the dispersed stray light is minimized, and the Thomson intensity is

20 September 2024 16:08:35

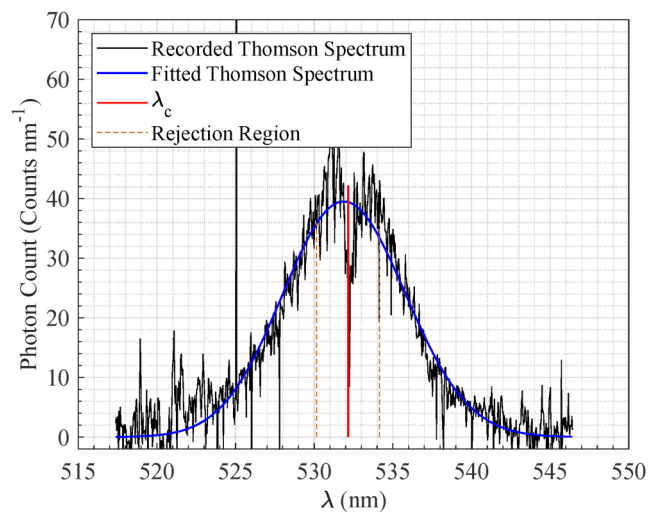


FIG. 7. Raw LTS spectrum and Thomson fit at 0.05 channel lengths downstream of the thruster exit plane and at the 3 o'clock azimuthal location.

maximized, such that the distortions to the LTS spectrum from the stray light are minimized. The Maxwellian fit agrees well with the raw spectrum in Fig. 7. There is some deviation from the Maxwellian fit at the lower wavelengths, but this spectral range coincides with emission lines that may have distorted the LTS spectrum if they were not subtracted properly. Consequently, it is appropriate to use the Maxwellian fit to analyze the collected data.

Electron density profiles

In Fig. 8, the measured electron density axial profiles generally follow the expected profile in the acceleration region, with the electron density dropping at a rate that decreases with distance from the ionization region.⁷ For 171 V, the maximum density is around $6.3 \times 10^{17} \text{ m}^{-3}$, and for 154 V, the maximum density is around $7.6 \times 10^{17} \text{ m}^{-3}$. For 171 V, the minimum density is around $1.3 \times 10^{17} \text{ m}^{-3}$, and for 154 V, the minimum density is around $1.4 \times 10^{17} \text{ m}^{-3}$. Throughout the profiles, the 154 V condition consistently has a higher electron density with few exceptions.

An increase in electron density in the acceleration region with a reduction in discharge voltage has been observed before,³⁸ which is the expected trend. The ion velocity should scale with $\sqrt{V_D}$, while the propellant utilization decreases at a slower rate with a decrease in discharge voltage.³⁹ At a constant mass flow rate, the ion current, thus, decreases slower with a decrease in discharge voltage than ion velocity does, such that the ion density increases with a reduced discharge voltage. Assuming quasineutrality, this confirms that we should expect an increase in electron density with a decrease in discharge voltage.

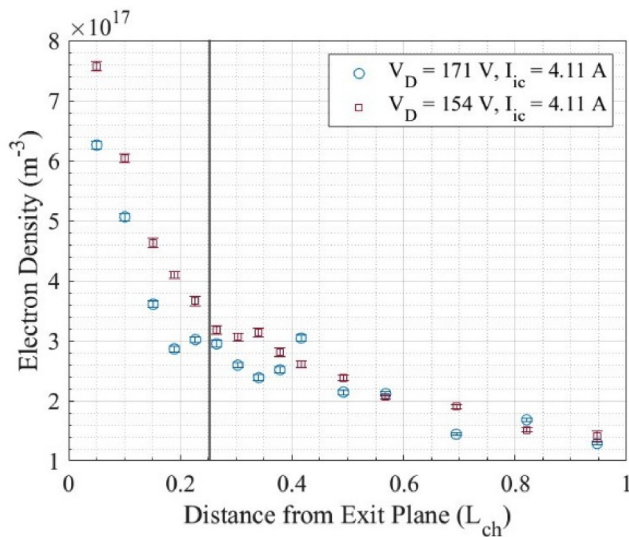


FIG. 8. Axial profile of the electron density for two different discharge voltages. The distance from the exit plane is normalized by the length of the discharge channel. The vertical line denotes the location of the maximum magnetic field strength. In addition to the error bars shown, all values of electron density are subject to 10% relative error that would affect all values in a similar manner.

In Fig. 9, the stronger magnetic field case has a higher density closer than 0.35 channel lengths downstream of the exit plane. In comparison, the baseline condition generally has a higher density farther than 0.35 channel lengths downstream of the exit plane. The low magnetic field case is the high discharge voltage case from Fig. 8. For the higher magnetic field strength case, the maximum density is around $7.4 \times 10^{17} \text{ m}^{-3}$, and the minimum density is around $1.4 \times 10^{17} \text{ m}^{-3}$.

To try to explain the observed differences between the discharge conditions in Fig. 9, we note that the magnetic field strength was optimized for the low magnetic case, such that the axial electron current should be near a minimum and, thus, not be a strong function of the magnetic field strength. A stronger magnetic field strength should decrease the azimuthal electron drift velocity via a decrease in the $E \times B$ velocity, and the axial electron drift velocity is related to the azimuthal electron drift velocity by⁴⁰

$$\Omega_e = \frac{v_{e\theta}}{v_{ez}}, \quad (16)$$

where Ω_e is the electron Hall parameter. However, while the axial profiles of the electron Hall parameter have been inferred from measurements and have been shown to have a strong peak,³⁻⁵ to the authors' knowledge, the axial profile of the Hall parameter has not been compared at two different magnetic field strengths. As a result, the expected behavior of electron density with a change in magnetic field strength is unclear.

It should be noted that for the electron density measurements provided, there is an additional 10% error due to the uncertainty in

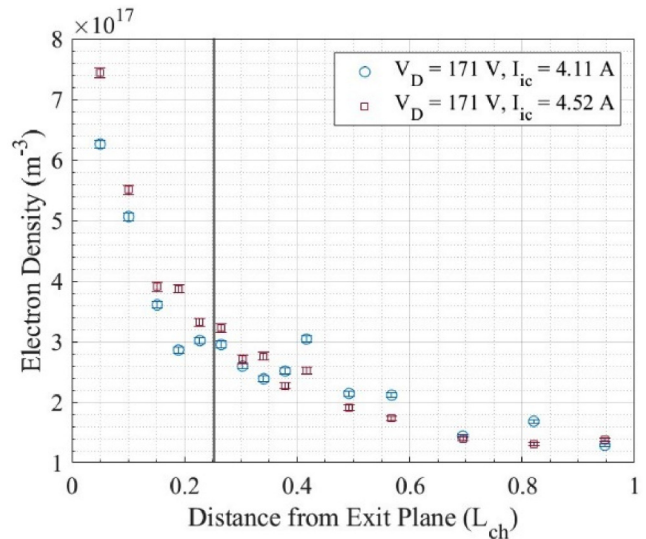


FIG. 9. Axial electron density profile for two different magnetic field strengths. The distance from the exit plane is normalized by the length of the discharge channel. The vertical line denotes the location of the maximum magnetic field strength. In addition to the error bars shown, all values of electron density are subject to 10% relative error that would affect all values in a similar manner.

20 September 2024, 16:08:35

the Raman cross sections of N_2 and O_2 .⁴¹ However, an error in the Raman cross sections would affect all the reported densities equally, so we decided not to plot this uncertainty to show the trends between the relative densities.

Electron temperature profiles

Figure 10 shows that the measured axial profiles of electron temperature profiles have the expected behavior of having a strong peak near the peak magnetic field strength. This is expected because joule heating is the primary source of electron heating⁴² combined with the electric field having a strong peak near the peak magnetic field strength,⁷ but this reasoning should be re-examined because LTS measures electron temperatures significantly higher than that predicted by Joule heating. Because the axial profile of electron temperature is closely tied to that of the electric field and because we observe the rise and fall of electron temperature, we can conclude that our LTS measurements span the entire axial extent of the acceleration region. The low discharge voltage plays a large role in shifting the peak electric field downstream. Indeed, in Ref. 28, LTS was able to measure across the entire acceleration region on a magnetically shielded HET operating at 150 V and at a nominal flow rate. However, it is unclear whether the relatively high flow rate used in this study also plays a large role in enabling LTS to access the entire acceleration region of the H9.

For the 171 V case, the maximum electron temperature is around 41.5 eV, and the minimum electron temperature is around 10 eV. For the 154 V case, the maximum electron temperature is around 37 eV, and the minimum electron temperature is around 9 eV. The 171 V case consistently has a higher electron temperature with few exceptions, but this trend is within the uncertainty at most axial

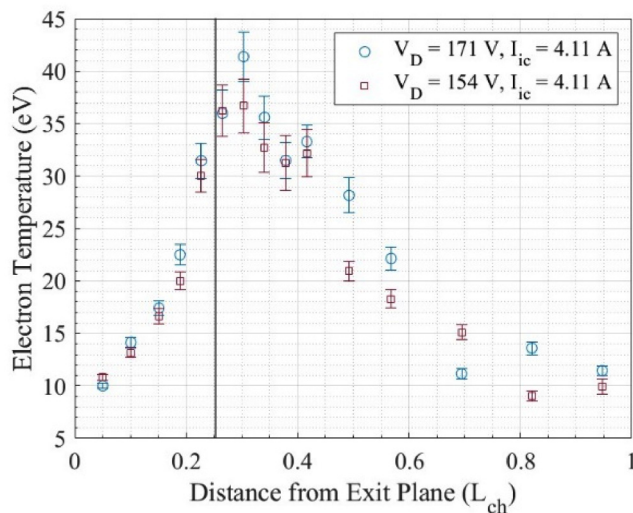


FIG. 10. Axial profile of the electron temperature for two different discharge voltages. The distance from the exit plane is normalized by the length of the discharge channel. The vertical line denotes the location of the maximum magnetic field strength.

locations. The reduction in the maximum electron temperature by 10% due to a 10% drop in the discharge voltage is also consistent with the electron temperature being proportional to the discharge voltage.¹

When operating a HET on xenon, the peak electron temperature is expected to be around 10% of the discharge voltage,¹ but we measured a peak temperature of approximately 25% of the discharge voltage. Even though we operated the H9 on krypton, we do not expect the electron temperature for krypton to be significantly higher than for xenon. In fact, LTS measurements have shown that operating a HET on krypton results in a lower electron temperature than when operating at the same condition but on xenon.³⁷

Other LTS measurements have also measured significantly larger electron temperatures than those expected.^{24,25,37} We can directly compare our electron temperature measurements at 154 V to the LTS measurements in Ref. 37 on a magnetically shielded HET operating at 150 V and on krypton. At this discharge condition in Ref. 37, the peak average of the azimuthal and radial temperatures is 30.5 eV, which is lower than our measurement of 37 eV at 154 V. The study in Ref. 37 operated at lower magnetic field strength than in this study, which could explain the lower electron temperature in Ref. 37. The study in Ref. 25 also presented measurements on the H9, and even though they ran the H9 at a different discharge current than in this study, they also measured a peak electron temperature of around 25% of the discharge voltage, with a discharge voltage of 300 V and a peak electron temperature of around 80 eV. Possible reasons for the discrepancy between LTS measurements and the expected electron temperature are the reliance on Langmuir probe data, and the fact that simulations calibrated on LIF data do not account for anomalous electron heating.^{6,7} Anomalous electron heating has been recently observed experimentally,⁴³ and the best practices for Langmuir probes in electric propulsion testing do not consider the impact of magnetized electrons on sheath theory, which could affect the reliability of Langmuir probe measurements in the acceleration region.^{23,24,44}

Figure 11 presents the electron temperature axial profiles for two different cases of magnetic field strength. The figure shows no clear trend between the electron temperature axial profiles at the two different field strengths. This observation is expected for small changes in the magnetic field strength around the optimum magnetic field strength because the electric field has been shown to have the strongest peak around the optimal magnetic field strength.²⁶ For the case of lower magnetic field strength, the maximum electron temperature is around 41.5 eV, and the minimum electron temperature is around 10 eV. For the case of higher magnetic field strength, the maximum electron temperature is around 40.5 eV, and the minimum electron temperature is around 10.5 eV. The slightly lower maximum electron temperature for our case of an increase in magnetic field strength could be explained by a higher magnetic field strength increasing the region in which the electron can be efficiently confined.²⁶ However, the uncertainties of the peak electron temperature for both magnetic field strengths overlap, such that no definitive conclusion can be made on which magnetic field strength as a higher peak electron temperature.

Figure 11 shows that the peak electron temperature shifts closer to the channel exit plane by one point within the axial profile. This is consistent with the trend seen in Refs. 19 and 26, that increasing the magnetic field strength shifted the peak electric

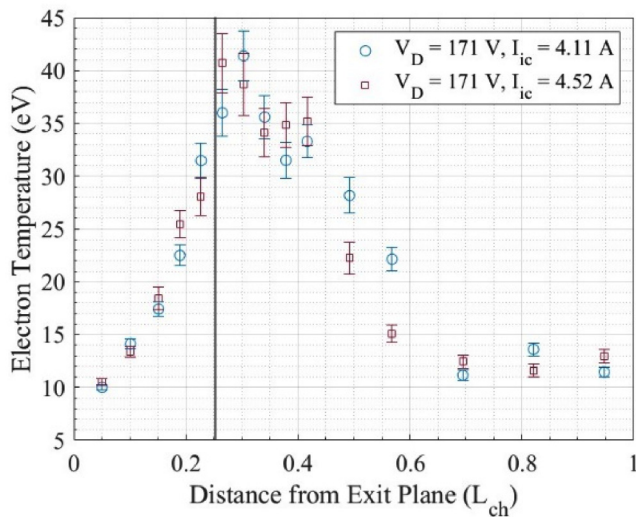


FIG. 11. Axial profile of the electron temperature for two different magnetic field strengths. The distance from the exit plane is normalized by the length of the discharge channel. The vertical line denotes the location of the maximum magnetic field strength.

field upstream. However, it is important to note that the location of the peak electron temperature for the high magnetic field case is within the uncertainty of the two highest temperatures. As a result, no definitive conclusion can be made on whether the stronger magnetic field shifts the peak electron temperature upstream.

Azimuthal electron drift velocity profile

Figure 12 shows that the peak magnitude of the azimuthal electron drift velocity is at the same location as the peak electron temperature for the same discharge condition. For an axial electric field and a radial magnetic field, the azimuthal electron drift velocity in the acceleration region should scale closely with $\frac{E_z}{B_r}$ because of the ExB velocity, where B_r is negative in our setup. In the acceleration region, the electric field has a significantly stronger axial gradient than the magnetic field,^{1,6,7} so we expect the axial profile of the azimuthal electron drift velocity to have a strong peak near the peak electric field. Because Fig. 12 shows the rise and fall of the azimuthal electric drift velocity, Fig. 12 corroborates the previous conclusion that the presented LTS measurements span the entire acceleration region.

The maximum measured azimuthal drift velocity has a magnitude of 680 km/s, which is lower than those previously measured with LTS.^{24,25,42} In Ref. 42, at the 150 V and krypton discharge condition, LTS measured a peak azimuthal electron drift velocity of around 820 km/s. The lower magnetic field strength at this discharge condition in Ref. 42 could explain the larger drift velocity even though the discharge voltage is around 10% lower than our discharge voltage. In Ref. 25, a peak azimuthal electron drift velocity of around 800 km/s was measured on the H9 at a discharge voltage of 300 V and operating on krypton. A lower azimuthal drift velocity is expected in our study given the lower discharge voltage, but we do not know the magnetic field strength used in Ref. 25.

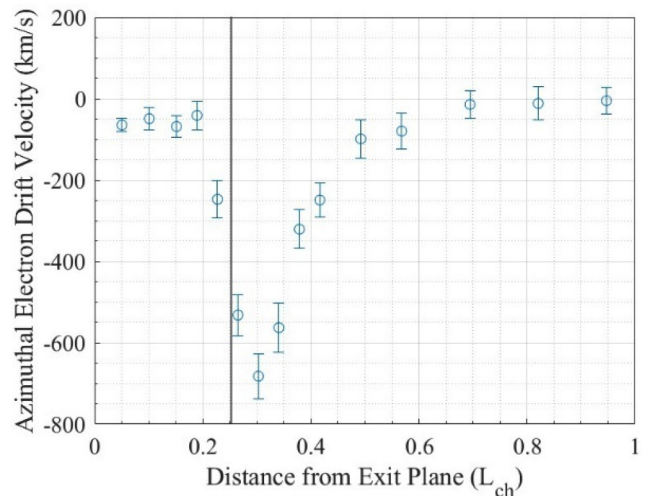


FIG. 12. Axial profile of the azimuthal electron drift velocity at the baseline discharge condition. The distance from the exit plane is normalized by the length of the discharge channel. The vertical line denotes the location of the maximum magnetic field strength.

DISCUSSION

Regarding the uncertainties in Figs. 8–12, the trend in uncertainties follows the expected trend. As per Eqs. (3)–(8), the LTS signal is proportional to the product of the electron density and the EVDF. The Maxwellian fit is more sensitive to values within a full-width-half-maximum (FWHM) of the Maxwellian 1D EVDF than values outside the FWHM. As a result, the uncertainty of the LTS results decreases as density decreases and as temperature increases. The points closest to the channel exit plane have the highest electron density and a low electron temperature, so these points have the lowest uncertainty. Because the density does not decrease as sharply downstream as it does upstream, the points with the highest temperature have a higher uncertainty than the points further downstream with a lower density. It will be important to increase the signal-to-noise ratio of our LTS system to provide lower uncertainties for the key electron properties, and a higher signal-to-noise ratio would also allow the system to operate at nominal thruster discharge conditions and at lower flow rates instead of the high current density conditions used in this study.

Having shown that our LTS diagnostic can measure the expected profiles of electron temperature and azimuthal electron drift velocity across the entire acceleration region, we can discuss a possible method for using LTS as a stand-alone diagnostic for calibrating simulations for both anomalous electron mobility and anomalous electron heating. Through Eq. (16), the axial profile of azimuthal electron drift velocity can be used in a one-equation experimental closure for the anomalous collision frequency in r - z fluid HET simulations like Ref. 45. The measured axial profile of electron temperature could then be simultaneously used to calibrate the anomalous electron heating in the simulation, which would also improve the accuracy of the axial electron pressure gradient. While the electron pressure could be calculated

in combination with the electron density from LTS measurements, we believe the electron density from such a simulation would not need further calibration if it were already calibrated on the azimuthal drift velocity and the electron temperature. The results of such a calibrated simulation would yield an axial profile of anomalous electron collision frequency and accurate electron properties, which would significantly help validate theories of anomalous electron mobility.

In addition, we note that to accurately model the axial electron pressure gradient in the expected case of anisotropic electron temperatures, the axial electron temperature is needed. However, current r - z fluid simulations of HET do not account for electron temperature anisotropy, so the calibration of these simulations with anisotropic electron temperatures is not straightforward. While the mixed azimuthal-radial electron temperature we measured is approximately representative of the average electron temperature that would be used in HET simulations that assume isotropic electron temperature, it is important to consider how to measure the axial electron temperature for accurate measurements of the axial pressure gradient.

We are aware of four possible approaches to measure or infer the axial electron temperature from LTS measurements in a HET. First, given that the azimuthal and axial direction are both approximately perpendicular to the magnetic field at the channel centerline, the azimuthal electron temperature should be a good measure of the axial electron temperature. However, we note that the presence of kinetic azimuthal instabilities is expected to distort the azimuthal EVDF but not the axial EVDF and that non-Maxwellian azimuthal EVDFs have been measured in Ref. 24. Second, we note that Eq. (11) is valid as long the electron pressure tensor has no off-diagonal components and that the electron temperatures are treated as effective electron temperatures. As a result, a LTS configuration with a subtended collection axis as in Fig. 1 could be used to make measurements at three azimuthal locations with different combinations of η_θ^2 and η_r^2 to solve a system of three equations for T_{ez} , $T_{e\theta}$, and T_{er} . To minimize the uncertainty in the inference of T_{ez} , the three azimuthal locations should correspond to the two locations used in Ref. 24 that were used to directly measure $T_{e\theta}$ and T_{er} and either the 3 o'clock, 9 o'clock, or 12 o'clock positions to measure at a location with $\eta_\theta^2 = \eta_r^2$. Third, to directly measure the axial EVDF would require an axial observation wavevector. This would require the incident wavevector to have an axial component, which would be challenging to implement and may require modifications to the HET to probe near the thruster exit plane. Finally, a mixed axial-azimuthal or axial-radial EVDF would be related to the convolution of the two 1D EVDFs, so signal processing techniques may be able to infer the axial EVDF from a mixed EVDF if the complementary EVDF is measured separately in a configuration without a subtended collection axis.

CONCLUSION

This paper presents LTS measurements of axial profiles of the electron density, electron temperature, and azimuthal electron drift velocity across the entire acceleration region of a HET. The shapes of the axial profiles agree with theory and are a further demonstration that magnetic shielding shifts the plasma downstream with respect to conventional HETs. We capture the expected results with a reduction in discharge voltage, namely, that the electron density increases and

that the electron temperature decreases proportionally to the drop in discharge voltage. The peak electron temperatures were around 25% of the discharge voltage, which supports previous LTS measurements of anomalous electron heating in the acceleration region of a HET. As demonstrated by the axial profiles of the electron temperature and the azimuthal electron drift velocity, the low discharge voltages of 171 and 154 V shift the acceleration region of H9 far enough downstream to provide LTS full optical access of the acceleration region. It is possible that the high flow rate also helps in providing LTS access to the entire acceleration region, but signal-to-noise ratio limitations prevented LTS measurements at lower flow rates. For future experiments, we plan to reduce the LTS system's detection limit to access H9 operating conditions with lower flow rates.

We have briefly discussed a method with which LTS data of electron temperature and azimuthal electron drift velocity can be used to directly calibrate r - z HET fluid codes for both anomalous electron mobility and anomalous electron heating. Consequently, LTS has the potential to be a stand-alone diagnostic for the validation of plasma properties in the acceleration region from HET simulations.

ACKNOWLEDGMENTS

This work was supported by a NASA Space Technology Graduate Research Opportunity (No. 80NSSC23K1217). The authors would like to thank Wensheng Huang, Dan Lev, Dongho Lee, and Jacob Knott for helpful discussions about the results and the rest of HPEPL for support during the experiment.

AUTHOR DECLARATIONS

Conflict of Interest

The authors have no conflicts to disclose.

Author Contributions

Julian Lopez-Uricoechea: Conceptualization (lead); Formal analysis (lead); Investigation (equal); Methodology (equal); Writing – original draft (lead); Writing – review & editing (supporting). **Jean Luis Suazo Betancourt:** Formal analysis (supporting); Investigation (equal); Methodology (lead). **Naia Butler-Craig:** Investigation (equal); Methodology (equal). **Mitchell L. R. Walker:** Conceptualization (supporting); Project administration (lead); Resources (lead); Writing – review & editing (lead).

DATA AVAILABILITY

The data that support the findings of this study are available from the corresponding author upon reasonable request.

REFERENCES

- ¹D. M. Goebel, I. Katz, and I. G. Mikellides, *Fundamentals of Electric Propulsion* (Wiley, 2023).
- ²I. D. Kaganovich, A. Smolyakov, Y. Raitsev, E. Ahedo, I. G. Mikellides, B. Jorns, F. Taccogna, R. Gueroult, S. Tsikata, A. Bourdon *et al.*, "Physics of $E \times B$ discharges relevant to plasma propulsion and similar technologies," *Phys. Plasmas* 27, 120601 (2020).
- ³N. B. Meezan, W. A. Hargus, Jr., and M. A. Cappelli, "Anomalous electron mobility in a coaxial Hall discharge plasma," *Phys. Rev. E* 63, 026410 (2001).

- ⁴J. A. Linnell and A. D. Gallimore, "Hall thruster electron motion characterization based on internal probe measurements," in *International Electric Propulsion Conference* (Electric Rocket Propulsion Society, 2009), IEPC-2009-105.
- ⁵E. T. Dale and B. A. Jorns, "Non-invasive time-resolved measurements of anomalous collision frequency in a Hall thruster," *Phys. Plasmas* **26**, 013516 (2019).
- ⁶I. G. Mikellides, A. Lopez Ortega, I. Katz, and B. A. Jorns, "Hall2de simulations with a first-principles electron transport model based on the electron cyclotron drift instability," in *52nd AIAA/SAE/ASEE Joint Propulsion Conference* (American Institute of Aeronautics and Astronautics, 2016), p. 4618.
- ⁷J. C. Adam, J. P. Boeuf, N. Dubuit, M. Dudeck, L. Garrigues, D. Gresillon, A. Heron, G. J. M. Hagelaar, V. Kulaev, N. Lemoine *et al.*, "Physics, simulation and diagnostics of Hall effect thrusters," *Plasma Phys. Controlled Fusion* **50**, 124041 (2008).
- ⁸S. Tsikata, N. Lemoine, V. Pisarev, and D. M. Gresillon, "Dispersion relations of electron density fluctuations in a Hall thruster plasma, observed by collective light scattering," *Phys. Plasma* **16**, 033506 (2009).
- ⁹Z. A. Brown and B. A. Jorns, "Spatial evolution of small wavelength fluctuations in a Hall thruster," *Phys. Plasmas* **26**, 113504 (2019).
- ¹⁰D. L. Brown, C. W. Larson, B. E. Beal, and A. D. Gallimore, "Methodology and historical perspective of a Hall thruster efficiency analysis," *J. Propul. Power* **25**, 1163–1177 (2009).
- ¹¹T. Lafleur, S. D. Baalrud, and P. Chabert, "Theory for the anomalous electron transport in Hall effect thrusters II. Kinetic Model," *Phys. Plasmas* **23**, 053503 (2016).
- ¹²B. Jorns, "Predictive, data-driven model for the anomalous electron collision frequency in a Hall effect thruster," *Plasma Sources Sci. Technol.* **27**, 104007 (2018).
- ¹³B. A. Jorns, "Two equation closure model for plasma turbulence in a Hall effect thruster," in *International Electric Propulsion Conference* (Electric Rocket Propulsion Society, 2019), IEPC-2019-129.
- ¹⁴T. A. Marks and B. A. Jorns, "Challenges with the self-consistent implementation of closure models for anomalous electron transport in fluid simulations of Hall thrusters," *Plasma Sources Sci. Technol.* **32**, 045016 (2023).
- ¹⁵S. Mazouffre, "Laser-induced fluorescence diagnostics of the cross-field discharge of Hall thrusters," *Plasma Sources Sci. Technol.* **22**, 013001 (2013).
- ¹⁶W. A. Hargus, Jr., and M. A. Cappelli, "Laser-induced fluorescence measurements of velocity within a Hall discharge," *Appl. Phys. B* **72**, 961–969 (2001).
- ¹⁷A. L. Fabris, C. V. Young, and M. A. Cappelli, "Time-resolved laser-induced fluorescence measurement of ion and neutral dynamics in a Hall thruster during ionization oscillations," *J. Appl. Phys.* **118**, 233301 (2015).
- ¹⁸R. Spektor, K. D. Diamant, E. J. Beiting, Y. Raitses, and N. J. Fisch, "Laser induced fluorescence measurements of the cylindrical Hall thruster plume," *Phys. Plasmas* **17**, 093502 (2010).
- ¹⁹V. H. Chaplin, B. A. Jorns, A. Lopez Ortega, I. G. Mikellides, R. W. Conversano, R. B. Lobbia, and R. R. Hofer, "Laser-induced fluorescence measurements of acceleration zone scaling in the 12.5 kW HERMeS Hall thruster," *J. Appl. Phys.* **124**, 183302 (2018).
- ²⁰W. Huang, B. Drenkov, and A. Gallimore, "Laser-induced fluorescence of singly-charged xenon inside a 6-kW Hall thruster," in *45th AIAA/ASME/SAE/ASEE Joint Propulsion Conference and Exhibit* (American Institute of Aeronautics and Astronautics, 2009), p. 5355.
- ²¹W. Huang and A. Gallimore, "Laser-induced fluorescence study of neutral xenon flow evolution inside a 6-kW Hall thruster," in *45th International Electric Propulsion Conference* (Electric Rocket Propulsion Society, 2009), IEPC-2009-087.
- ²²T. Wegner, S. J. Thompson, J. Williams, and A. P. Yalin, "Two-photon absorption laser induced fluorescence (TALIF) of neutral xenon in a Hall effect thruster plasma," in *AIAA Propulsion and Energy 2021 Forum* (American Institute of Aeronautics and Astronautics, 2021), AIAA-2021-3301.
- ²³R. B. Lobbia and B. E. Beal, "Recommended practice for use of Langmuir probes in electric propulsion testing," *J. Propul. Power* **33**, 566 (2017).
- ²⁴B. Vincent, S. Tsikata, and S. Mazouffre, "Incoherent Thomson scattering measurements of electron properties in a conventional and magnetically-shielded Hall thruster," *Plasma Sources Sci. Technol.* **29**, 035015 (2020).
- ²⁵P. J. Roberts and B. A. Jorns, "Laser measurement of anomalous electron diffusion in a crossed-field plasma," *Phys. Rev. Lett.* **132**, 135301 (2024).
- ²⁶D. Gawron, S. Mazouffre, N. Sadeghi, and A. Heron, "Influence of magnetic field and discharge voltage on the acceleration layer features in a Hall effect thruster," *Plasma Sources Sci. Technol.* **17**, 025001 (2008).
- ²⁷I. G. Mikellides, I. Katz, R. R. Hofer, and D. M. Goebel, "Magnetic shielding of a laboratory Hall thruster. I. Theory and validation," *J. Appl. Phys.* **115**, 043303 (2014).
- ²⁸B. Vincent, S. Tsikata, S. Mazouffre, and C. Boniface, "Thomson scattering investigations of a low-power Hall thruster in standard and magnetically-shielded configurations," in *International Electric Propulsion Conference* (Electric Rocket Propulsion Society, 2019), IEPC-2019-384.
- ²⁹J. L. Suazo Betancourt, N. Butler-Craig, J. Lopez-Uricoechea, J. Bak, D. Lee, A. M. Steinberg, and M. L. R. Walker, "Thomson scattering measurements in the krypton plume of a lanthanum hexaboride hollow cathode in a large vacuum test facility," *J. Appl. Phys.* **135**, 083302 (2024).
- ³⁰R. R. Hofer, "The H9 magnetically shielded Hall thruster," in *International Electric Propulsion Conference* (Electric Rocket Propulsion Society, 2017), IEPC-2017-232.
- ³¹M. Sekerak, R. Hofer, J. Polk, B. W. Longmier, A. Gallimore, D. L. Brown, "Mode transitions in Hall effect thrusters," in *49th AIAA/ASME/SAE/ASEE Joint Propulsion Conference* (American Institute of Aeronautics and Astronautics, 2013), p. 4116.
- ³²M. Sekerak, B. Longmier, A. Gallimore, W. Huang, H. Kamhawi, R. Hofer, B. Jorns, and J. Polk, "Mode transitions in magnetically shielded Hall effect thrusters," in *50th AIAA/ASME/SAE/ASEE Joint Propulsion Conference* (American Institute of Aeronautics and Astronautics, 2014), p. 3511.
- ³³J. Sheffield, D. Froula, S. H. Glenzer, and N. C. Luhmann, Jr., *Plasma Scattering of Electromagnetic Radiation: Theory and Measurement Techniques* (Elsevier Science, 2018).
- ³⁴J. L. Suazo Betancourt, J. Lopez-Uricoechea, N. Butler-Craig, A. Steinberg, and M. L. R. Walker, "An incoherent thomson scattering system for measurements near plasma boundaries," *Rev. Sci. Instrum.* **95**, 043001 (2024).
- ³⁵M. J. van de Sande and J. J. A. M. van der Mullen, "Thomson scattering on a Low-pressure, inductively-coupled gas discharge lamp," *J. Phys. D: Appl. Phys.* **35**, 1381 (2002).
- ³⁶J. Bak, J. L. Suazo Betancourt, A. Rekhy, A. Abbasszadehrad, R. B. Miles, C. M. Limbach, and M. L. R. Walker, "High-resolution spatially extended 1D laser scattering diagnostics using volume Bragg grating notch filters," *Rev. Sci. Instrum.* **94**, 023003 (2023).
- ³⁷B. Vincent, "Incoherent thomson scattering investigations in Hall thruster, planar magnetron and ECR Ion source plasmas," Ph.D. dissertation (Université D'Orléans, 2019).
- ³⁸N. Z. Warner, J. J. Szabo, and M. Martinez-Sanchez, "Characterization of a high specific impulse Hall thruster using electrostatic probes," in *International Electric Propulsion Conference* (Electric Rocket Propulsion Society, 2003), IEPC-2003-082.
- ³⁹Y. Raitses, J. Ashkenazy, and M. Guelman, "Propellant utilization in Hall thrusters," *J. Propul. Power* **14**, 247–253 (1998).
- ⁴⁰J. P. Boeuf, "Tutorial: Physics and modeling of Hall thrusters," *J. Appl. Phys.* **121**, 011101 (2017).
- ⁴¹C. M. Penney, R. L. St. Peters, and M. Lapp, "Absolute rotational Raman cross sections for N₂, O₂, and CO₂," *J. Opt. Soc. Am.* **64**, 712–716 (1974).
- ⁴²I. G. Mikellides and A. Lopez Ortega, "Challenges in the development and verification of first-principles models in Hall-effect thruster simulations that are based on anomalous resistivity and generalized Ohm's law," *Plasma Sources Sci. Technol.* **28**, 014003 (2019).
- ⁴³P. J. Roberts, and B. Jorns, "Inferring electron heat flux in a high-power Hall thruster with incoherent Thomson scattering," in *AIAA SCITECH 2024* (American Institute of Aeronautics and Astronautics, 2024), p. 1957.
- ⁴⁴P. J. Ryan, J. W. Bradley, and M. D. Bowden, "Comparison of Langmuir probe and laser Thomson scattering for electron property measurements in magnetron discharges," *Phys. Plasmas* **26**, 073515 (2019).
- ⁴⁵I. G. Mikellides and I. Katz, "Numerical simulations of Hall-effect plasma accelerators on a magnetic-field-aligned mesh," *Phys. Rev. E* **86**, 046703 (2012).